Detecting gravitational waves sources − BHBH, NSNS, BHNS − with LISA

Nazeela Aimen, Syed Ali Mohsin Bukhari, Asad Ali

Department of Applied Mathematics and Statistics, Institute of Space Technology, Islamabad 44000, Pakistan.
Space and Astrophysics Research Lab (SARL), Institute of Space Technology, Islamabad 44000, Pakistan.

Abstract—The double compact objects (DCOs) present a broad range of possible GW detections in our MW galaxy. Here we present a case study on the detection of DCOs with progenitors having high metallic content. Furthermore, the effects of eccentricity on the ZAMS stage on the evolution of binaries is also checked via a comparative analysis for two identical data sets. The binaries were generated using the Compact Object Mergers: Population Astrophysics and Statistics (COMPAS) suite, followed by their distribution in a metallicity−age dependent Milky Way galaxy model.

For a 4-year LISA mission, this study predicts a detection rate between 79-127(86-131) detections for data sets with variable ZAMS and zero ZAMS eccentricity respectively. Out of these, 21-45(17-36) are BHBHs, 17-44(17-38) are NSNSs, 6-28(11-29) are BHNSs and 13-39(21-46) are NSBHs. NSBH were considered separate from BHNS as the stellar evolution indicates that the primary star in the binary ended up as a NS instead of a BH. It was also observed that some common binaries end up in different DCO stages in both data sets.

Index Terms—Gravitational waves, gravitational wave detectors, black holes, neutron stars, double compact objects

I. INTRODUCTION

The gravitational waves (GW) were predicted a year after the final formulation of the general theory of relativity (GR) by Albert Einstein [18]. Similar to electromagnetic waves, the GWs travel at the speed of light [1, 17]. However, unlike electromagnetic waves, the GW stretches and squeezes the space itself thus causing spatial disturbances. The detection of Hulse-Taylor binary [25], and the subsequent observation of a seven years time span [49] stirred a great interest in the GW observations. It wasn't until 2015 that the first direct observation of GW was made by LIGO and VIRGO collaborations [1]. The lower frequency bound for both the aLIGO and VIRGO detectors is around $10\,\text{Hz}$ [2, 15]

The Laser Interferometer Space Antenna (LISA) has three spacecrafts that form a triangle, each side 2.5 million km long [39, 43]. Operating in the frequency range of $1 \times 10^{-5}\,\text{Hz} \leq f \leq 1 \times 10^{-1}\,\text{Hz}$ LISA will be able to observe the sources millions of years before they merge. The early detection capability will help better constrain and determine the orbital parameters of the observed binaries. Some sources detectable by LISA are the extreme mass ratio inspirals (EMRIs) [14, 23, 29] and galactic binaries [1, 16, 52]. This makes LISA also capable of mapping Milky Way galaxy's structure. Another interesting class detectable by LISA is the double white dwarf stars (DWDs) which are reported to be abundant in our MW galaxy and have a substantial detection in LISA as well [30, 35, 44, 54].

A lot of effort has been put into the detection of potential GW sources for LISA, the resolution of issues that might be associated with the background data, and proposals of new candidates as GW sources for LISA [see, for example, 3, 4, 5, 8, 9, 13, 22, 24, 28, 32, 35, 40, 44, 46, 47, 52, 55]. The detections of these sources will provide us with a better understanding of not only the evolution phases but also the endpoints of stellar evolution.

The goals of this research are,

1) to predict the number of DCO binaries that can be detected via LISA in our Milky Way galaxy,
   a) to determine whether extra galactic sources are LISA detectable,
2) to make a general detection comparison between DCO binaries with and without an initial eccentricity.

This research paper is structured as follows, in section II we discuss the generation of binary systems using COMPAS suite. In section III we give a general overview of the methodology adopted in this research for evolving the stars from ZAMS to DCOs, from DCOs to merger stage, and their detection by LISA as well. The evolution of binaries and their detection is discussed in section IV.

II. POPULATION SYNTHESIS

The population synthesis for the detections of the double compact objects (DCOs) was performed using the Compact Object Mergers: Population Astrophysics and Statistics (COMPAS; [42, 48, 50]) suite. COMPAS is a rapid stellar evolution suite and can evolve both single and binary stars following the details outlined by [26, 27]. A list of selected papers that make use of the COMPAS suite is also available on the COMPAS website.[1]

This study makes use exclusively of the binary star evolution (BSE) synthesis method. The default parameters used by the COMPAS software are listed in table 1 in the COMPAS paper [42].

Except for supernova mass remnant prescription, initial eccentricity (e_i), metallicity (z), and pulsar evolution, all other parameters were taken at the default value. For a one-to-one correspondence between the two generated data sets, the seed numbers were kept constant.

---

[1] https://compas.science/science.html

For the mass of primary star, we draw the values from Kroupa initial mass function (IMF) with $m_1 \in [5, 150] \, \mathrm{M_\odot}$ [31]. For the secondary star, we randomly draw from uniform distribution to satisfy $q \equiv m_2/m_1$, where $q \in [0, 1]$ [45]. An additional constraint of $m_2 \geq 0.1 \, m_1$ was placed on m_2 as this is the minimum mass necessary for a star to be considered as a main sequence star.

For the semi-major axis of the binary, we drew the parameter values from a flat-in-the-log distribution with $a_i \in [0.1, 1000]$ AU, such that $p(a_i) \propto 1/a_i$ [36].

For the remnant mass prescription, we first considered the Fryer delayed model [21]. However, this resulted in a concentration of NS mass around $\sim 1.28 \, \mathrm{M_\odot}$. To avoid this concentration of NS final mass, we used Müller & Mandel prescription (M&M) [33]. M&M is a stochastic remnant mass model that offers a smoother mass distribution for NS. We also switched the **evolve_pulsar** flag to **True** during population synthesis.

For metallicity, we drew the values from a Beta$(5, 80)$ distribution. The main motivation behind the selection of such biased distribution is the higher metallic content of present-day stars. The population III stars were primarily composed of pure hydrogen and their deaths produced heavier metals in the Universe. By this extension, the stars that are present now or those that will merge now must have higher metallic content. As such, we also speculate that having stars with higher metallic content might produce more NSNS or NS-BH pairs for detection rather than BHBH pairs.

For eccentricity, we make use of two cases,

- Case I: All the binary systems are generated using a uniform distribution, $e \in (0, 1]$.
- Case II: All the binary systems are generated with circular orbits, i.e., $e = 0$.

From here on the data set for Case I and Case II will be represented by Θ_1 and Θ_2 respectively. Details about the selection of metallicity and eccentricity values in COMPAS are provided in appendix A.

III. EVOLUTION METHODOLOGY

We first generated 1×10^7 values for metallicity using the beta distribution within the COMPAS limits. We denote the zero-age main sequence (ZAMS) parameters of the binaries as,

$$m_{1_{\mathrm{ZAMS}}}, m_{2_{\mathrm{ZAMS}}}, a_{\mathrm{ZAMS}}, e_{\mathrm{ZAMS}}, Z, \varnothing \tag{1}$$

COMPAS evolves the binaries up to $13.7 \, \mathrm{Gyr}$. We represent the resulting double compact object (DCO) parameters as,

$$m_{1_{\mathrm{DCO}}}, m_{2_{\mathrm{DCO}}}, a_{\mathrm{DCO}}, e_{\mathrm{DCO}}, t_{\mathrm{evolve}}, Z, \varnothing, \tag{2}$$

where Z is the metallicity of the binary system, $\varnothing$ is the seed number, t_{evolve} is the time required to form DCO from ZAMS. a_{ZAMS}, a_{DCO}, e_{ZAMS}, and e_{DCO} are the semi-major axis and eccentricity of the binary orbit at ZAMS and DCO formation respectively. Once the DCOs have been formed, we move out of the COMPAS suite. For the LISA detection, the DCO formed from the set of binaries were checked for an evolutionary stop, i.e., only those binaries were selected that
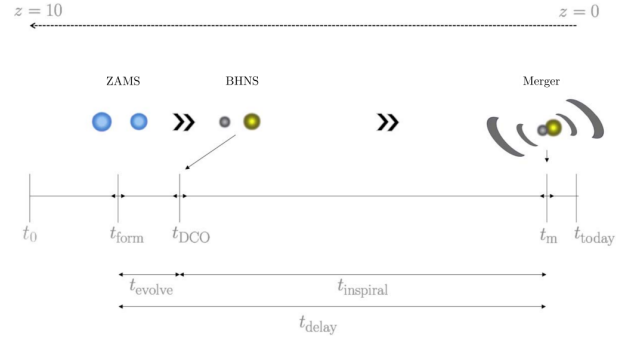

Fig. 1: Schematic diagram showing various time intervals for a binary system from ZAMS formation, to DCO, and merger. The figure is taken from [42].

will merge within the Hubble time. The selected candidates were than provided to the python framework LEGWORK [51] that evolved them from the DCO stage to the merger state. It evolved the binaries using equations from [37, 38].

The DCO$-$merger evolution method follows the one outlined by [52] closely. The evolution was done such that the MW galaxy instance was divided into bins based on the metallicity values of the evolving binaries. The evolution time was calculated after taking into consideration the ZAMS-DCO evolution time and the lookback time of all the MW points within the metallicity bins. If a binary, at DCO stage, had a resultant merger time greater than the difference of its lookback time and ZAMS-DCO evolution time, it was marked as an inspiralling binary. Each inspiralling binary was than evolved at every point within the corresponding metallicity bin using LEGWORK to a million year before its merger time. At this stage, the resulting LISA parameters of interest were,

$$a_{\mathrm{LISA}}, e_{\mathrm{LISA}}, f_{\mathrm{LISA}} \tag{3}$$

The SNR was than calculated by further evolving them for the LISA mission duration of four years. The detection is made based on the signal-to-noise ratio (SNR) of the binary averaged over sky position, polarization, and orientation using the following expression from [19],

$$\rho^2 = \sum_{n=1}^{\infty} \int_{f_{n,i}}^{f_{n,f}} \frac{h_{c,n}^2}{f_n^2 S_n(f_n)} \, \mathrm{d}f_n, \tag{4}$$

where n is the GW harmonic, f_n represents the orbital frequency of nth harmonic. The parameter $S_n(f_n)$ is the LISA sensitivity curve function [43], and $h_{c,n}$ is the characteristic strain of the nth GW harmonic [6].

$$h_{c,n}^2 = \frac{2^{5/3}}{3\pi^{4/3}} \frac{(G\mathcal{M}_c)^{5/3}}{c^3 D_L^2} \frac{1}{f_{\mathrm{orb}}^{1/3}} \frac{g(n,e)}{nF(e)} \tag{5}$$

IV. EVOLUTION AND DETECTION

After running the simulations as outlined in section II, we obtained 12254 DCOs ($\sim 0.12254\%$). Following section III, we obtain the required parameter values of only 6539 DCOs that merged within Hubble time ($\sim 53.3622\%$) thus making

them a potential LISA source.[2] The Hubble time merge rate of DCOs is given in table I,

Type	BHBH	NSNS	BHNS	
			NSBH	BHNS
M/T	$492/663$	$4752/9219$	$480/868$	$815/1504$
D/M	$348/492$	$1281/4752$	$329/480$	$330/815$

TABLE I: **RowI** shows the merging (M) vs total (T) formed DCOs in this study, **RowII** shows the uniquely detectable (D) vs the merging (MR) DCOs from this study for Θ_1.

The highest merging rate in this study is of BHBH pairs ($\sim74.21\%$), followed by NSBH pairs ($\sim55.30\%$), BHNS ($\sim54.2\%$) and lastly NSNS DCO type ($\sim51.55\%$) comprising the 'candidate binaries'.[3]

Using the LEGWORK framework [51], these binaries were than checked for their inspiral phase using the t_{evolve}[4] and $t_{lookback}$[5]. The difference between lookback and evolution time of a binary was required to be greater than its merger time[6]. Out of the merging binaries, BHBH pairs had the most detectable sources in the data set, ($\sim70.73\%$), followed by NSBH pair ($\sim68.54\%$), BHNS pair ($\sim40.49\%$) and lastly NSNS pair ($\sim26.96\%$).

As the number of detectable binaries in our study was small compared to the total generated population,[7] multiple detections of a single binary object are present in the final output. Table II shows selective details about mass of progenitor and their evolutionary ends for maximum and minimum mass at ZAMS and DCO stages. In appendix C we present the number of detection and mean values for selected parameters[8] across the hundred instances of MW galaxies. The number of detections across all the MW instances came out to be 12758.

The predicted distribution of the LISA detectable sources is plotted over its expected sensitivity curve [43], in figure 2. The x-axis shows the dominant frequency, the frequency accumulating the largest SNR, for the eccentric binaries. Furthermore, on y-axis we plot the amplitude spectral density (ASD), including the contribution from all harmonics. The gap between the detected binaries and the LISA curve in the graph is the SNR criteria, (SNR > 7). The size of the points varies with metallicity; high metallic sources have larger shapes and vice versa. The color scheme is based on the eccentricity of detected binaries with a reverse red-yellow-green color palette[9], going from green, yellow and finally red in increasing order of eccentricity values.

[2]Overall, only $\sim0.06539\%$ binary system formed into DCOs that merge within Hubble time.

[3]Such DCO pairs which can have a potential LISA detection.

[4]Obtained via COMPAS.

[5]Obtained via galaxy synthesis.

[6]Obtained via LEGWORK framework.

[7]Due to not using any technique that forces DCO production, e.g., STROOPWAFEL [12]

[8]The selected parameters include, $m_{1_{DCO}}$, $m_{2_{DCO}}$, a_{DCO}, e_{DCO}, Z, t_{evol}, $t_{lookback}$, and SNR.

[9]https://matplotlib.org/stable/gallery/color/colormap_reference.html

Parameters	MAX	ZAMS details		DCO details		MIN	ZAMS details		DCO details	
		Primary	Secondary	Primary	Secondary		Primary	Secondary	Primary	Secondary
Binary Black Holes										
$m_{1_{ZAMS}}$	149.836	149.836	115.624	10.386	10.395	13.007	13.007	12.500	2.216	2.601
$m_{2_{ZAMS}}$	131.178	148.802	131.178	8.662	8.459	12.500	13.007	12.500	2.216	2.601
$m_{1_{DCO}}$	43.308	57.334	57.334	43.308	43.308	2.022	26.497	26.493	2.022	7.104
$m_{2_{DCO}}$	43.308	57.334	57.334	43.308	43.308	2.018	42.088	30.574	7.456	2.018
Binary Neutron Stars										
$m_{1_{ZAMS}}$	54.41	54.41	13.76	1.614	1.235	8.546	8.546	7.822	1.26	1.193
$m_{2_{ZAMS}}$	25.571	25.586	25.571	1.480	1.693	6.626	13.01	6.626	1.26	1.194
$m_{1_{DCO}}$	1.938	14.022	13.938	1.938	1.487	1.135	10.319	10.019	1.135	1.392
$m_{2_{DCO}}$	1.991	13.919	13.574	1.681	1.991	1.132	11.674	11.021	1.518	1.132
Neutron Star − Black Hole										
$m_{1_{ZAMS}}$	53.708	53.708	29.613	1.439	15.342	8.971	8.971	8.847	1.260	3.869
$m_{2_{ZAMS}}$	42.242	42.289	42.242	1.598	7.382	8.665	9.164	8.665	1.260	2.062
$m_{1_{DCO}}$	1.935	14.090	13.959	1.935	3.825	1.137	27.186	17.676	1.137	9.646
$m_{2_{DCO}}$	15.342	53.708	29.613	1.439	15.342	2.003	12.472	12.033	1.608	2.003
Black Hole − Neutron Star										
$m_{1_{ZAMS}}$	145.467	145.467	46.439	9.907	1.593	11.626	11.626	11.608	2.216	1.522
$m_{2_{ZAMS}}$	108.489	140.091	108.489	12.217	1.415	10.072	23.144	10.072	2.922	1.206
$m_{1_{DCO}}$	15.106	90.844	76.11	15.106	1.669	2.004	13.125	12.872	2.004	1.785
$m_{2_{DCO}}$	1.945	29.142	15.445	4.341	1.945	1.141	28.317	22.834	5.61	1.141

TABLE II: Maximum and minimum values for masses of both ZAMS and DCO type stars in the BHBH data set with their respective counterparts. The 'MAX' and 'MIN' columns represent the maximum and minimum value for the given parameter respectively. The 'ZAMS details' and 'DCO details' column list the value of primary and secondary components of the binary and respective stage of evolution with 'MAX' and 'MIN' value of the parameter at that stage. All the masses are given in units of solar mass, $M_\odot$ where $1\,M_\odot \approx 2 \times 10^{30}$ kg.
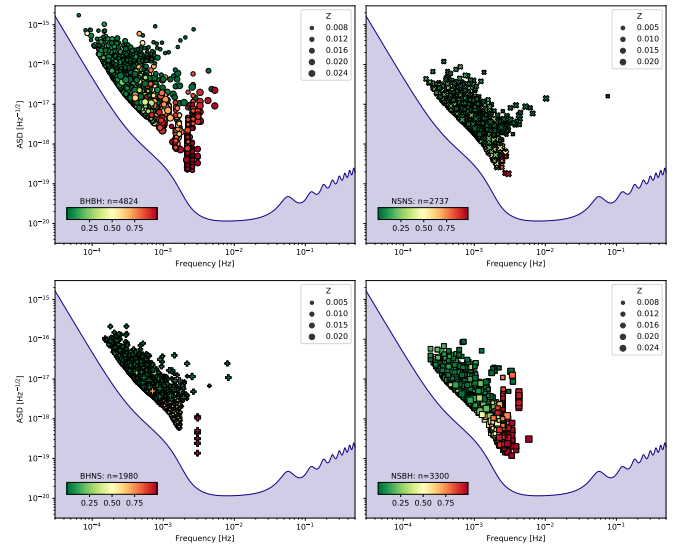

Fig. 2: Detectable sources' characteristic strain vs. dominant frequency in our simulations are shown on the LISA sensitivity curve. The sources are color-coded based on their eccentricities, green for low and red for high eccentric sources.

Majority of the binary population reside on the lower end of LISA spectrum, e.g., the dominant frequency of the sources lie below the LISA's sensitive frequency of $10\,$mHz. For TEXT**Row1**, the peak frequency occurs at 174×10^{-6} $174\,\mu$Hz, $530.8\,\mu$Hz Majority of the binary population for all DCO types have a dominant frequency towards the lower end of the LISA spectrum, e.g., dominant frequency is less than 1×10^{-2} Hz, (see figure 3 **Row2**). The main reason for such a trend can be explained through the eccentricities of the binaries. As seen from the figure 3 **Row3**, a large portion of our binaries is either low or mid-eccentric. The
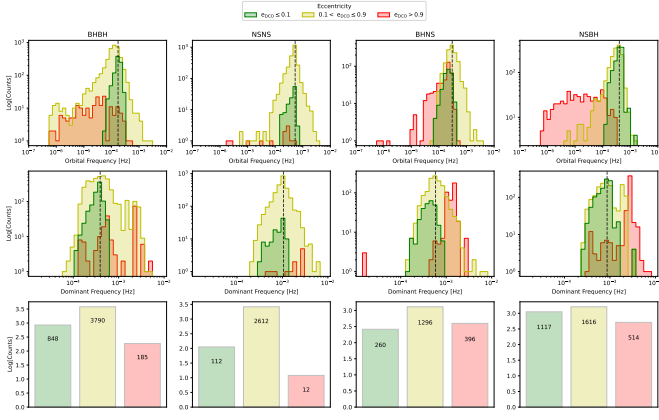
Fig. 3: **Row1:** Eccentricity characterized distribution of DCOs for their orbital frequency. **Row2:** Same as **Row1** but for the binary's dominant frequency. **Row3:** Number of binaries associated with the given eccentricity in log scale. The number inside the bars show the actual number of binaries for the given eccentricity. The log scaling was chosen due to relative lower number of DCOs in NSNS and BHNS types.

orbit of low eccentric or circular binaries evolves differently than high eccentric binaries. After the formation of DCO, most of the low eccentric binaries emit GW in low-frequency bands of LISA as the orbit progresses. While DCOs with high eccentricities behave in a completely different way, i.e. their orbit decay faster, and they tend to emit GW in high harmonics [37, 38]. Fig. 3 **Row1** shows the distribution of population over their orbital frequency; f_{orb}. We can see from orbital and dominant frequency histograms that although no DCO with $e > 0.9$ had $f_{\mathrm{orb}} > 1 \times 10^{-3}$ Hz but due to their large SNR harmonics the dominant frequency for a lot of those binaries shift upwards of 1×10^{-3} Hz which pushes them to LISA's more sensitive region.

Figure 4 shows the percentage of different DCOs detected in the low-$[\alpha/\mathrm{Fe}]$, high-$[\alpha/\mathrm{Fe}]$ and bulge components of the MW instances. For low-$[\alpha/\mathrm{Fe}]$ disk, the NSBH pairs have more detections than BHN pairs. Contrary to that, NSBH pairs show no detection in high-$[\alpha/\mathrm{Fe}]$ disk, and fractional detection in the bulge, $\sim 0.833\%$. On the other hand, the BHNS pairs have the lowest detection rate in all three components.

Figure 5 shows the percentage of detections in the three components regardless of the DCO type. Here we see that majority of the detections are in the low-$[\alpha/\mathrm{Fe}]$ disk. This can be attributed to the biased metallicity value used in this study, $\mathrm{Beta}(5, 80)$. These detection percentages do align with the age-metallicity relationship as the bulge is oldest component and thus should have lower metallicity ZAMS stars. However, due to the choice of metallicity distribution, these stars were not generated in large numbers.

A. Maximum distance

For each DCO, there is a horizon distance i.e., the maximum distance up to which the DCO may be detectable in LISA. This
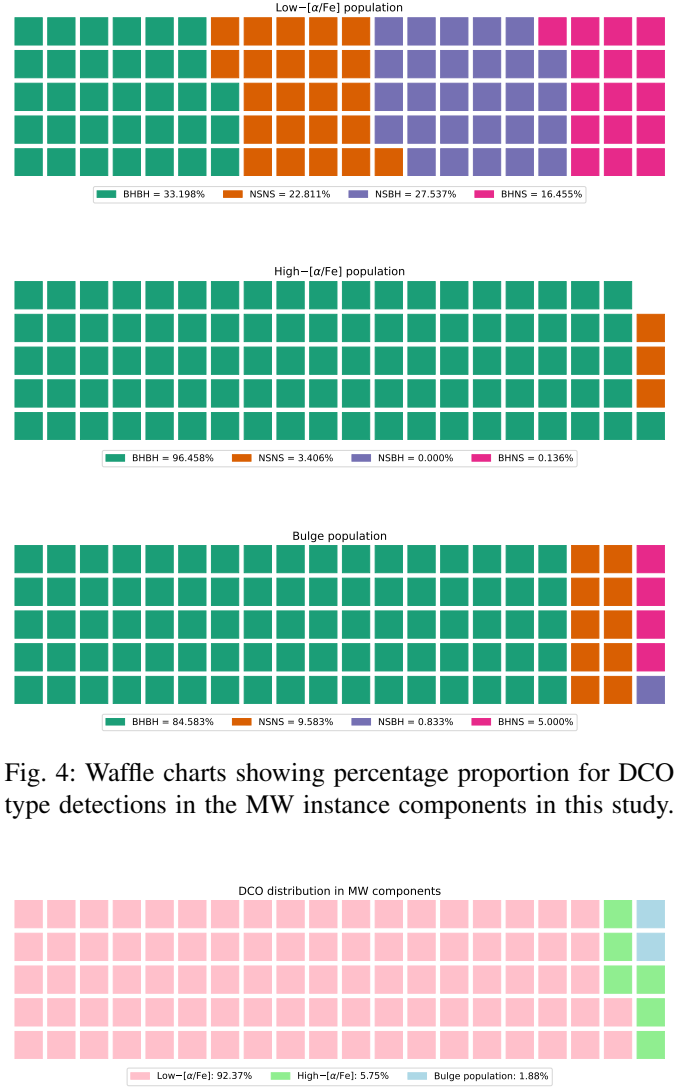

Fig. 4: Waffle charts showing percentage proportion for DCO type detections in the MW instance components in this study.
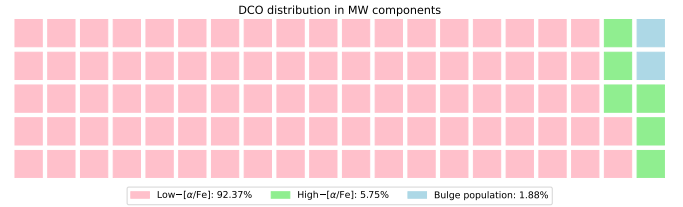

Fig. 5: Waffle chart showing the total number of detections per MW instance component in this study on the whole.

is calculated using the inverse relationship between SNR (ρ) and distance [32],

$$d_{\max} = \frac{\rho(d = 1\,\mathrm{kpc})}{\rho_{\min}} \qquad (6)$$

Where $\rho_{\min}$ is the minimum value of SNR below which the source is not detectable. We keep the detection threshold at $\rho_{\min} = 7$, and $\rho(d = 1\,\mathrm{kpc})$ is SNR of the source if it was at $1\,\mathrm{kpc}$ distance from the detector. We calculated the SNR of all the detected sources at $1\,\mathrm{kpc}$ distance using the python package LEGWORK [51]. Afterward, their maximum distances ($d_{\max}$) were calculated.

Figure 6 shows the mean maximum distances for all the detected sources. The black line shows the average maximum distance for all the types combined. The LISA sensitivity curve is also overlaid on the graph.

BHBH, being the dominant source can be observed to an average distance of more than 1×10^5 kpc. NSBH and BHNS have almost the same average $d_{\max}$ i.e between 1×10^3 kpc
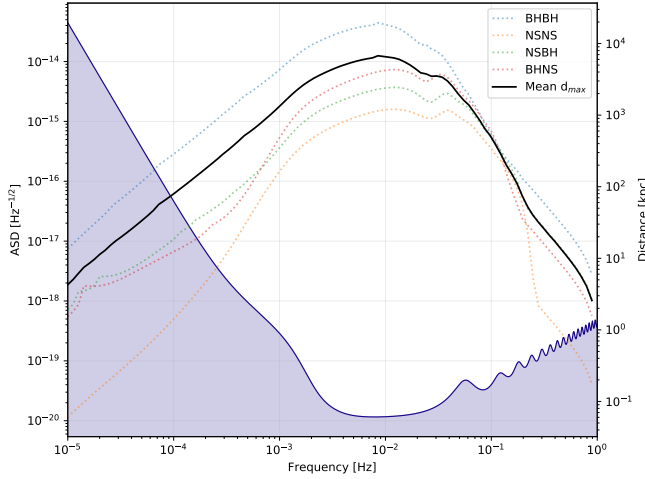
Fig. 6: Mean maximum distances for all of the different types of DCO corresponding to their orbital frequency. The overall average maximum detection distance is shown by a black line.

and 1×10^4 kpc while NSNS has peak at $\sim 1 \times 10^3$ kpc. The red dotted lines illustrate some known galaxies to have a better understanding of distances. Hence, BHBH can be discovered as far as Hoag's Object, NSNS in M31, and both BHNS and NSBH are far from M31 but much below Hoag's Object.

Almost all the highest values of average $d_{\max}$ of four types are around a **certain frequency** i.e., if a source has **certain orbital frequency** then it can be detected to its maximum detection distance. It can be observed through the LISA overlay that this frequency lies in the area where the detector is most sensitive. Hence, if a source emits in the frequency region of the highest sensitivity of LISA, then it will be detected at a maximum distance.

V. COMPARATIVE ANALYSIS

In this section, we will deal with the comparative study of our eccentric binary data set $(\aleph_1)$ with circular binary data set, $(\aleph_2)$. In order to fairly compare the outputs of the two data sets, given only the difference of eccentricity, we make use of the seed numbers provided in $\aleph_1$ data set. With the exception of SN kick parameters and eccentricity, all the other parameters were kept the same as in $\aleph_1$. We evolved the binaries consistent with the method described in this paper.

A. Hubble Merger Rate

After running the simulations, we obtained 9751 DCO pairs ($\sim 0.09751\%$). Out of these, only 5178 ($\sim 53.1022\%$) were able to merge within Hubble time. Table III shows the proportion of DCO merger for each DCO type for $\aleph_2$ data set.

Like the $\aleph_1$ data set, the highest merging rate for $\aleph_2$ comes from BHBH as well ($\sim 66.32\%$), followed by BHNS pairs ($\sim 65.87\%$), NSBH ($\sim 63.03\%$) and lastly, NSNS dco type ($\sim 51.57\%$).

BHBH	NSNS	BHNS	
		NSBH	BHNS
189/285	4438/8605	193/293	385/568

TABLE III: Number of DCOs merged within Hubble time vs total DCOs formed by the COMPAS suite for circular binary data set.

B. Effects of eccentricity

A total of 140 seeds were found common between the two data sets. Out of these 140 seeds, 105 were found to evolve to the same final stage before merging. The binaries with common and diverging final evolutionary stages are shown in figure 7. The lesser number of diverging cases indicate that the ZAMS eccentricity might not play as much of a bigger role in the evolution of the binaries.

C. Detection rates

The prediction for VE is a total of 136 detections in a 4 years LISA mission. A decrease in the detection rate is observed for E0 which is detected in a 4 years LISA mission. As there is no difference in any parameter other than eccentricity, then it is surely the root cause of the decline in detections.

The difference in different types of sources is shown in the pie chart in which there is a clear reduction in the detected sources. **Explain the pie chart more**

D. Model variation: To be added somewhere else,

In a number of previous works, e_{ZAMS} was taken as zero [7, 13, 32, 50, 52]. The main reason for this assumption is that they argue that eccentricity at ZAMS is not likely critical for predicting detection rates as they deal with post-interaction binaries and their orbital eccentricities become zero after mass transfer [27]. To test the accuracy of this assumption, we simulate another population with the same parameters. The only change is that e_{ZAMS} of the binaries is left to be varied by the COMPAS suite. We compare the difference in detection rates and properties of the two models and give our conclusion.
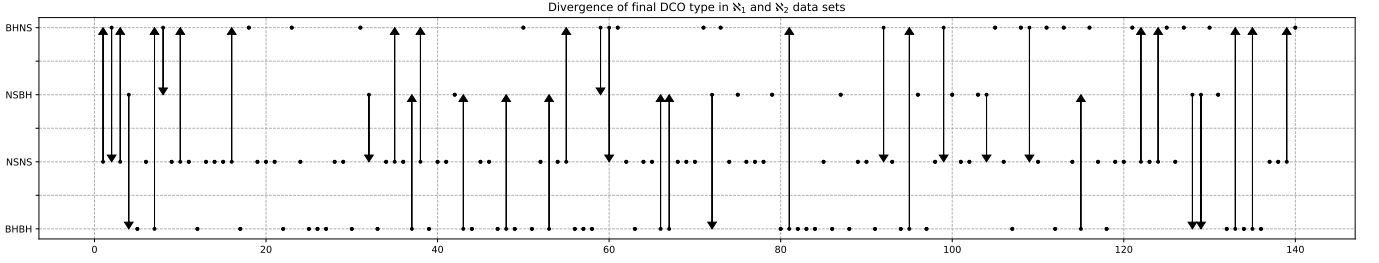
VI. DISCUSSION AND FUTURE WORK

Fig. 7: Plot showing the change in DCO ending states for the common seed numbers from $\aleph_1$ and $\aleph_2$ data sets. The direction of arrows shows the change in the DCO type from $\aleph_1$ and $\aleph_2$ data set. The binaries that didn't change the DCO type after evolution are represented by a filled dot.
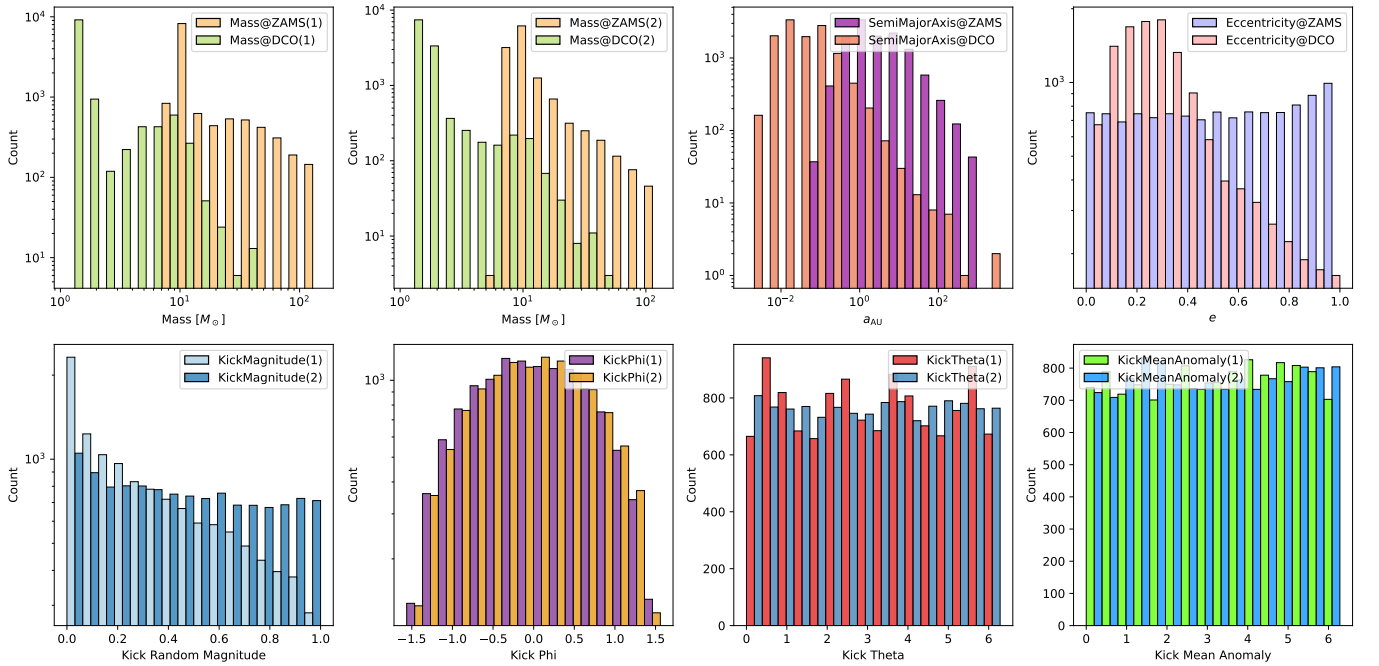

Fig. 8: The top row shows the distribution of mass, semimajor axis and eccentricity of binary pairs at ZAMS and DCO stage for the 'candidate' binaries. The bottom row shows the selection of supernova kick parameters made by the COMPAS suite.

REFERENCES

[1] Abbott, B. P., Abbott, R., Abbott, T. D., et al. 2017, ApJ, 848, L13, doi: 10.3847/2041-8213/aa920c

[2] Acernese, F. a., Agathos, M., Agatsuma, K., et al. 2014, Classical and Quantum Gravity, 32, 024001

[3] Andrews, J. J., Breivik, K., Pankow, C., D'Orazio, D. J., & Safarzadeh, M. 2020, ApJ, 892, L9, doi: 10.3847/2041-8213/ab5b9a

[4] Babak, S., Baker, J. G., Benacquista, M. J., et al. 2008, Classical and Quantum Gravity, 25, 114037

[5] —. 2010, Classical and Quantum Gravity, 27, 084009

[6] Barack, L., & Cutler, C. 2004, Phys. Rev. D, 69, 082005, doi: 10.1103/PhysRevD.69.082005

[7] Barrett, J. W., Gaebel, S. M., Neijssel, C. J., et al. 2018, MNRAS, 477, 4685

[8] Belczynski, K., Benacquista, M., & Bulik, T. 2010, ApJ, 725, 816, doi: 10.1088/0004-637X/725/1/816

[9] Błaut, A., Babak, S., & Królak, A. 2010, Phys. Rev. D, 81, 063008

[10] Bovy, J., Leung, H. W., Hunt, J. A. S., et al. 2019, MNRAS, 490, 4740, doi: 10.1093/mnras/stz2891

[11] Bovy, J., Rix, H.-W., Schlafly, E. F., et al. 2016, ApJ, 823, 30, doi: 10.3847/0004-637X/823/1/30

[12] Broekgaarden, F. S., Justham, S., de Mink, S. E., et al. 2019, MNRAS, 490, 5228

[13] Broekgaarden, F. S., Berger, E., Neijssel, C. J., et al. 2021, MNRAS, 508, 5028, doi: 10.1093/mnras/stab2716

[14] Chapman-Bird, C. E. A., Berry, C. P. L., & Woan, G. 2022, arXiv e-prints, arXiv:2212.06166

[15] Collaboration, L. S., & Aasi, J. 2015, Class. Quantum Gravity, 32, 074001

[16] Digman, M. C., & Hirata, C. M. 2022, arXiv e-prints, arXiv:2212.14887

[17] Eddington, A. S. 1922, Proceedings of the Royal Society of London Series A, 102, 268

[18] Einstein, A. 1916, Sitzungsberichte der Königlich Preußischen Akademie der Wissenschaften (Berlin), 688

[19] Finn, L. S., & Thorne, K. S. 2000, Phys. Rev. D, 62, 124021, doi: 10.1103/PhysRevD.62.124021

[20] Frankel, N., Rix, H.-W., Ting, Y.-S., Ness, M., & Hogg, D. W. 2018, ApJ, 865, 96, doi: 10.3847/1538-4357/aadba5

[21] Fryer, C. L., Belczynski, K., Wiktorowicz, G., et al. 2012, ApJ, 749, 91

[22] Fumagalli, J., Pieroni, M., Renaux-Petel, S., & Witkowski, L. T. 2022, JCAP, 2022, 020, doi: 10.1088/1475-7516/2022/07/020

[23] Gair, J. R., Babak, S., Sesana, A., et al. 2017, in Journal of Physics Conference Series, Vol. 840, Journal of Physics Conference Series, 012021

[24] Guo, H.-K., Shu, J., & Zhao, Y. 2017, arXiv e-prints, arXiv:1709.03500

[25] Hulse, R. A., & Taylor, J. H. 1975, ApJ, 195, L51

[26] Hurley, J. R., Pols, O. R., & Tout, C. A. 2000, MNRAS, 315, 543

[27] Hurley, J. R., Tout, C. A., & Pols, O. R. 2002, MNRAS, 329, 897

[28] Khakhaleva-Li, Z., & Hogan, C. J. 2020, arXiv, arXiv:2006.00438, arXiv: 2006.00438

[29] Klein, A., Barausse, E., Sesana, A., et al. 2016, Phys. Rev. D, 93, 024003

[30] Korol, V., Rossi, E. M., & Groot, P. J. 2017, in Astronomical Society of the Pacific Conference Series, Vol. 509, 20th European White Dwarf Workshop, ed. P. E. Tremblay, B. Gaensicke, & T. Marsh, 529

[31] Kroupa, P. 2001, MNRAS, 322, 231, doi: 10.1046/j.1365-8711.2001.04022.x

[32] Lau, M. Y. M., Mandel, I., Vigna-Gómez, A., et al. 2020, MNRAS, 492, 3061, doi: 10.1093/mnras/staa002

[33] Mandel, I., & Müller, B. 2020, MNRAS, 499, 3214

[34] McMillan, P. J. 2011, MNRAS, 414, 2446, doi: 10.1111/j.1365-2966.2011.18564.x

[35] Nelemans, G., Yungelson, L. R., & Portegies Zwart, S. F. 2001, A&A, 375, 890

[36] Öpik, E. 1924, Publications of the Tartu Astrofizica Observatory, 25, 1

[37] Peters, P. C. 1964, Physical Review, 136, 1224, doi:

10.1103/PhysRev.136.B1224

[38] Peters, P. C., & Mathews, J. 1963, Physical Review, 131, 435, doi: 10.1103/PhysRev.131.435

[39] Prince, T. A., Tinto, M., Larson, S. L., & Armstrong, J. W. 2002, Phys. Rev. D, 66, 122002, doi: 10.1103/PhysRevD.66.122002

[40] Renzo, M., Callister, T., Chatziioannou, K., et al. 2021, ApJ, 919, 128, doi: 10.3847/1538-4357/ac1110

[41] Riley, J., Mandel, I., Marchant, P., et al. 2021, MNRAS, 505, 663

[42] Riley, J., Agrawal, P., Barrett, J. W., et al. 2022, ApJS, 258, 34, doi: 10.3847/1538-4365/ac416c

[43] Robson, T., Cornish, N. J., & Liu, C. 2019, Classical and Quantum Gravity, 36, 105011, doi: 10.1088/1361-6382/ab1101

[44] Ruiter, A. J., Belczynski, K., Benacquista, M., Larson, S. L., & Williams, G. 2010, ApJ, 717, 1006

[45] Sana, H., de Mink, S. E., de Koter, A., et al. 2012, Science, 337, 444, doi: 10.1126/science.1223344

[46] Sesana, A., Volonteri, M., & Haardt, F. 2009, Classical and Quantum Gravity, 26, 094033, doi: 10.1088/0264-9381/26/9/094033

[47] Shao, Y., & Li, X.-D. 2021, ApJ, 920, 81, doi: 10.3847/1538-4357/ac173e

[48] Stevenson, S., Vigna-Gómez, A., Mandel, I., et al. 2017, Nat. Commun., 8, 14906, doi: 10.1038/ncomms14906

[49] Taylor, J. H., & Weisberg, J. M. 1982, ApJ, 253, 908

[50] Vigna-Gómez, A., Neijssel, C. J., Stevenson, S., et al. 2018, MNRAS, 481, 4009

[51] Wagg, T., Breivik, K., & de Mink, S. E. 2022, ApJS, 260, 52, doi: 10.3847/1538-4365/ac5c52

[52] Wagg, T., Broekgaarden, F. S., de Mink, S. E., et al. 2021, arXiv e-prints, arXiv:2111.13704, arXiv: 2111.13704

[53] Wegg, C., Gerhard, O., & Portail, M. 2015, MNRAS, 450, 4050

[54] Willems, B., Kalogera, V., Vecchio, A., et al. 2007, ApJ, 665, L59

[55] Yu, S., & Jeffery, C. S. 2010, A&A, 521, A85

APPENDIX A
SETTINGS FOR USING COMPAS

To generate a binary systems, COMPAS requires the following parameters from the user as discussed earlier,

- mass of primary star $(m_{1_{\text{ZAMS}}})$,
- mass of secondary star $(m_{2_{\text{ZAMS}}})$,
- semi-major axis of the orbit (a_{ZAMS}),
- random seed $(\emptyset)$
- remnant mass prescription,
- eccentricity of the orbit (e_{ZAMS}), and
- metallicity of the stars (Z).

We've discussed the first four parameters in the main text, here we will discuss the selection of eccentricity and metallicity values.

ECCENTRICITY

In order to evaluate whether the initial eccentricity affects GW emission at the end stages of the DCO, we generate two identical data sets. For the primary data set, we chose the eccentricity value to be varied between 0 and 1.

However, we noticed that some stars within the population synthesis had a ZAMS stellar type of 16. This refers to chemically homogeneously evolving stars [41, 42]. These binaries were found to have zero eccentricity even when the parameter was chosen to be within the range $(0, 1)$.

For the other data set we take the eccentricity value to be 0 for all the generated binaries.

METALLICITY

One of the major challenges in generation of the stellar binaries for this study was the selection of a distribution which will result in stars at the higher end of COMPAS metallicity boundary, $z = 0.03$. A power-law, gamma, and beta distributions were selected to try and simulate the required metallicity distribution. In the following section, we discuss the selected distributions briefly,

A. Power law distribution

The random values for metallicity were generated using the power law distribution given below,

$$f(x, a) = ax^{(a-1)} \tag{7}$$

where a is the index of the power law distribution.[10] Figure 9 shows the plot for the probability density function (PDF) of the power law with $a \in [1, 2]$. Although the distribution can produce higher values, it does not suppress the lower values so this distribution was discarded.

B. Gamma distribution

For the probability density function for gamma distribution,[11] we use the following form,

$$f(x, a) = \frac{x^{a-1} \exp(-x)}{\Gamma(a)} \tag{8}$$

for $x \geq 0$ and $a > 0$. Here, a is the shape factor, and Γ is the gamma function, such that $\Gamma(a) = (a - 1)!$. Similar to the power law distribution, the gamma distribution (see, figure 10) was not a good selection for the values of metallicity that were required for this study.
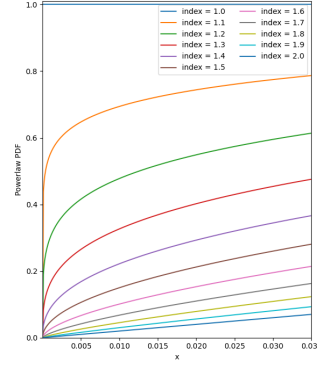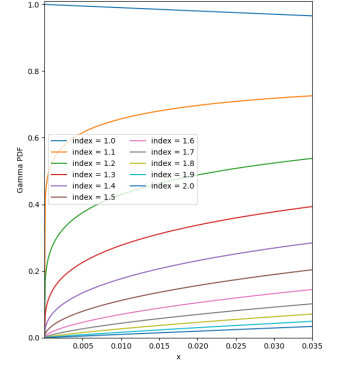

Fig. 9: PL distribution

Fig. 10: Γ distribution

C. Beta distribution

For the beta distribution, we use the following form,

$$f(x, a, b) = \frac{\Gamma(a + b)x^{a-1}(1 - x)^{b-1}}{\Gamma(a)\Gamma(b)} \tag{9}$$

For $0 \leq x \leq 1, a > 0, b > 0$ and Γ is the gamma function.[12]

Figure 11 shows the beta distribution with a fixed $\beta = 80$. Similarly, figure 12 shows the beta distribution with a fixed $\alpha = 5$. For our case, we selected $\text{Beta}(5, 80)$ as our distribution of choice for metallicity and generated 10^7 values between the COMPAS limits $10^{-4} < z < 0.03$.
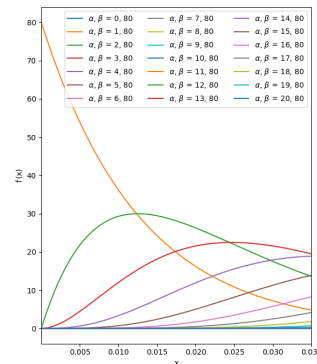

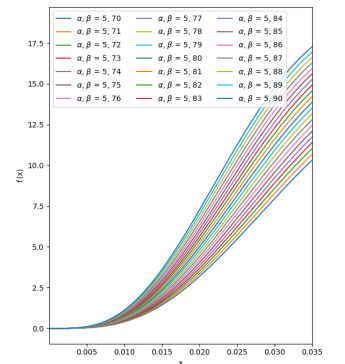Fig. 11: Beta distribution with varying α and fixed β parameter.

Fig. 12: Beta distribution with fixed α and varying β parameter.

APPENDIX B

THE MILKY WAY MODEL

In this section, we will briefly outline the milky way galaxy model used in this study. The model is developed by [52] and makes use of the galaxy's enrichment history by taking into account the metallicity-radius-time relationship [20]. It uses a separate star formation history and spatial distribution for the low-[α/Fe], high-[α/Fe] discs, and bulge in the galaxy.

A. Star formation rate

The star formation rate for both the low-[α/Fe] and high-[α/Fe] disks is expressed as,

$$p(\tau) \propto \exp\left(-\frac{\tau_m - \tau}{\tau_{\text{SFR}}}\right), \tag{10}$$

where τ is the time difference between the star's ZAMS stage and today. The age of milky way galaxy, τ_m, is taken as 12 Gyr, and the star formation rate as, $\tau_{\text{SFR}} = 6.8$ Gyr. The star-forming period of low-[α/Fe] and high-[α/Fe] discs were taken as 0 Gyr to 8 Gyr and 8 Gyr to 12 Gyr respectively. The model adopts 6 Gyr to 12 Gyr as the star-forming period of the bulge [10].

B. Radial distribution

The radial distribution of stars within the milky way galaxy was performed using the following expression,

$$p(R) = \exp\left(-\frac{R}{R_d}\right)\frac{R}{R_d^2} \tag{11}$$

However, a different scale length, R_d, was chosen for each component of the galaxy. For low-[α/Fe], the model uses $R_{\text{exp}}(\tau)$ as the scale length [20, Eq 6], where

$$R_{\text{exp}}(\tau) = 4\,\text{kpc}\left[1 - \alpha_{R_{\text{exp}}}\left(\frac{\tau}{8\,\text{Gyr}}\right)\right], \tag{12}$$

with the value of inside-out growth parameter, $\alpha_{R_{\text{exp}}}$, as 0.3. For high-[α/Fe] disc and bulge, the value of scale length was chosen as $(1/0.43)$ kpc and 1.5 kpc respectively.

C. Vertical distribution

The model employs a similar method of single exponent expression with varying scale height parameters for the vertical distribution as well. The exponential expression used is,

$$p(|z|) = \frac{1}{z_d}\exp\left(-\frac{z}{z_d}\right), \tag{13}$$

where z here is the vertical displacement from the galactic plane. The scale height parameter, z_d, for low-[α/Fe], high-[α/Fe] and bulge was taken as 0.3 kpc [34], 0.95 kpc [11], and 0.2 kpc [53] respectively.

D. Metallicity-radius-time relationship

The MRT relationship plays an important part, both in the galaxy model and later on in the placement of DCOs within the galaxy as well. The model makes use of [20, Eq. 7],

$$\begin{aligned}
[\text{Fe/H}](R, \tau) = F_m + \nabla[\text{Fe/H}]R \\
- \left(F_m + \nabla[\text{Fe/H}]R_{[\text{Fe/H}]=0}^{\text{now}}\right)f(\tau)
\end{aligned} \tag{14}$$

For each point generated, if the value of metallicity produced by the MW model was less or greater than the limits defined by COMPAS[13] it was changed to a uniformly drawn random number between COMPAS$_{\text{min}}$ − ZSOLAR and ZSOLAR − COMPAS$_{\text{max}}$ respectively.

E. Galaxy synthesis

For the synthesis of an instance of the Milky Way galaxy, the model described previously samples the following parameters,

$$\theta_i = \{\tau, D, z, \text{component}\},$$

where τ is the look-back time for the binary, D is the distance from Earth, z is the metallicity, and 'component' is the component of the galaxy in which the binary resides.[14] The parameters are generated for $i = 1, 2, 3, \ldots, N_{\text{GAL}}$, where $N_{\text{GAL}} = 100$.

[13]0.0001, 0.03

[14]One of the three, low-[α/Fe] disc, high-[α/Fe] disc, or bulge.

APPENDIX C
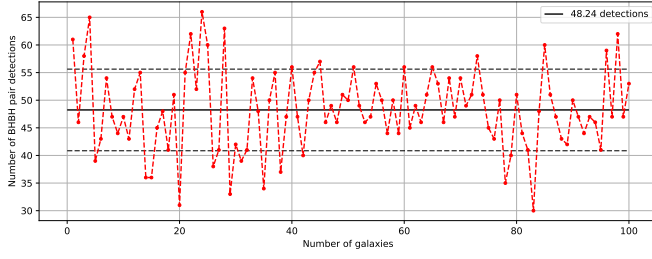## PARAMETER DISTRIBUTION ACROSS THE GALAXIES

A. Binary Black Holes

Fig. 13: Number of BHBH pair detection per galaxy instance. On average, a total of ~48 pairs per galaxy were detected in this study.
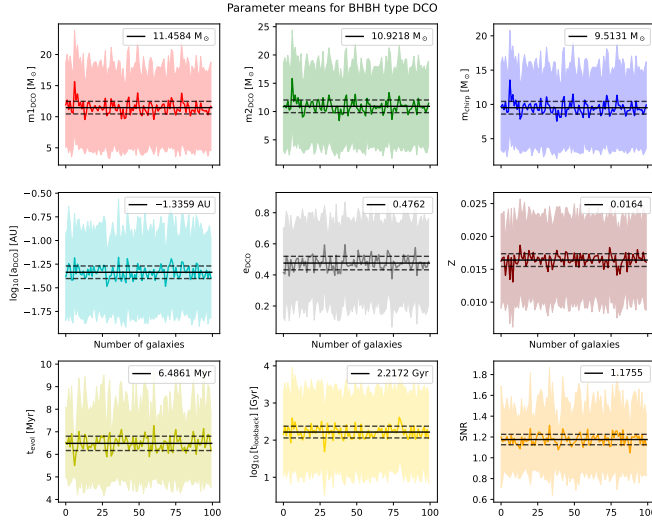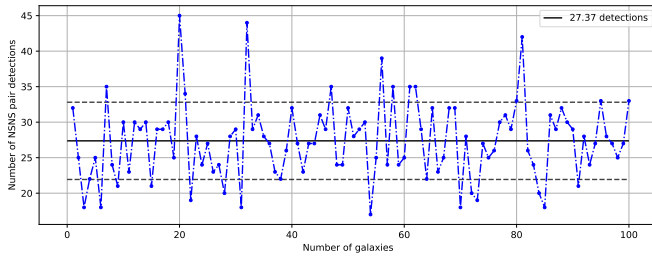

Fig. 14: The mean and standard deviation for selected parameters in every galaxy, plotted against the galaxy number. An overall measure of mean and standard deviation of all the galaxies is also shown for the selected parameter with a black solid and dashed lines respectively.

B. Binary Neutron Stars

Fig. 15: Number of NSNS pair detection per galaxy instance. On average, a total of ~27 pairs per galaxy were detected in this study.
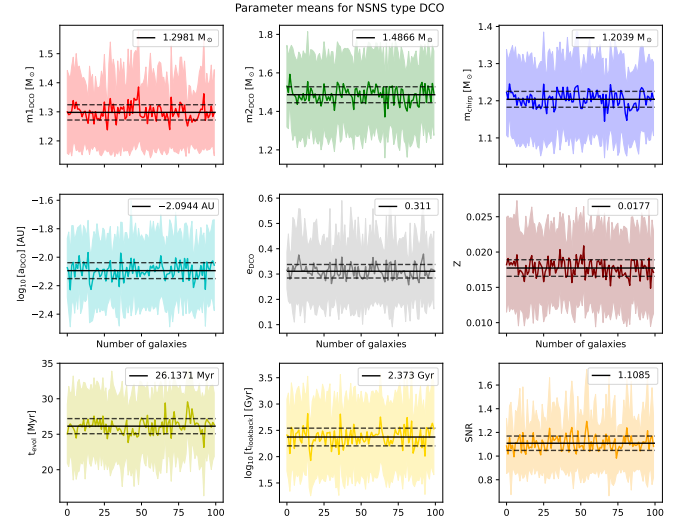
Fig. 16: Same as figure 14.

C. Neutron Star − Black Hole binary

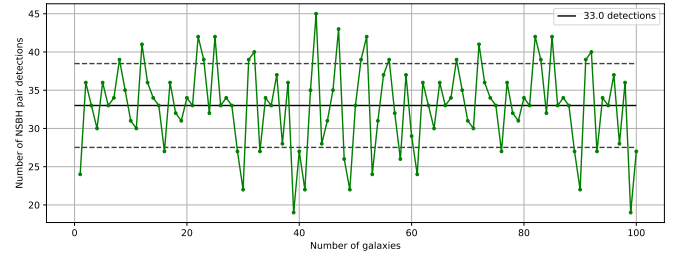

Fig. 17: Number of NSBH pair detection per galaxy instance. On average, a total of ~33 pairs per galaxy were detected in this study.
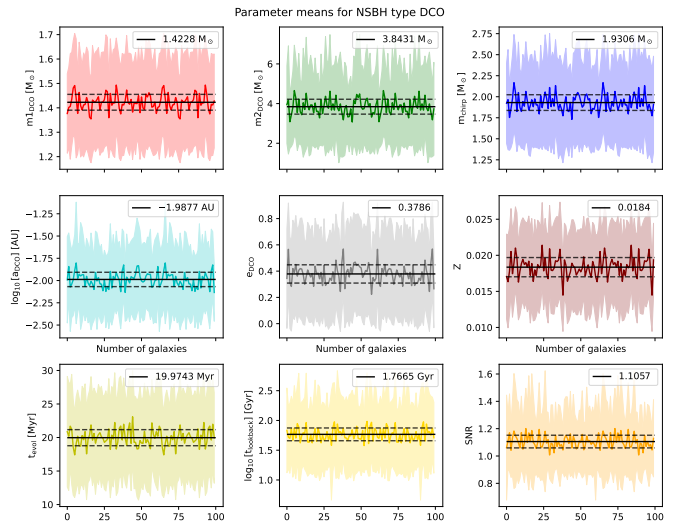

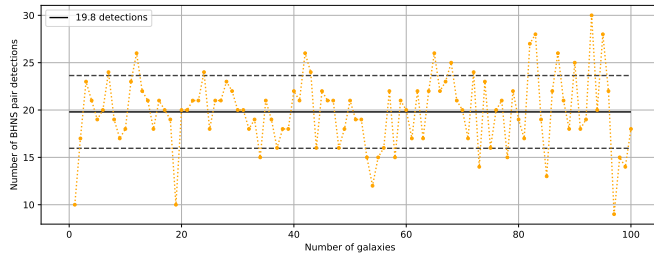Fig. 18: Same as figure 14.

D. Black Hole − Neutron Star binary

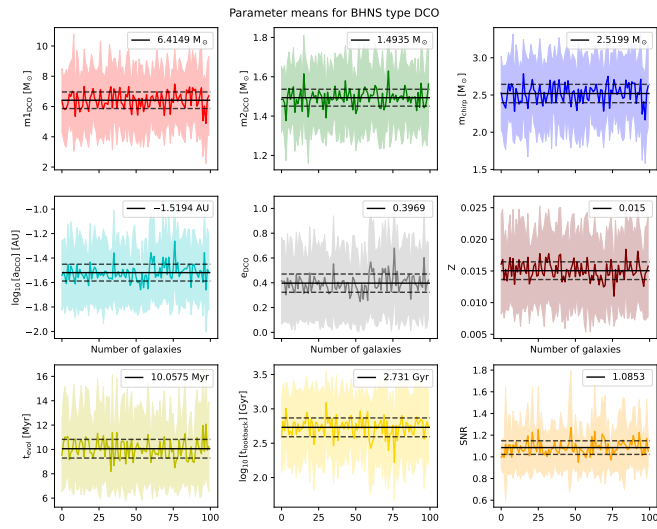Fig. 19: Number of BHNS pair detection per galaxy instance. On average, a total of ∼20 pairs per galaxy were detected in this study.

Fig. 20: Same as figure 14.